

## Molecular Mechanisms of Crystallization and Defect Formation

S.-T. Yau,<sup>1</sup> Bill R. Thomas,<sup>1,2</sup> and Peter G. Vekilov<sup>1,3,\*</sup>

<sup>1</sup>Center for Microgravity and Materials Research, University of Alabama in Huntsville, Huntsville, Alabama 35899

<sup>2</sup>Universities Space Research Association, AMMSA, Marshall Space Flight Center, Alabama 35812

<sup>3</sup>Department of Chemistry, University of Alabama in Huntsville, Huntsville, Alabama 35899

(Received 30 November 1999)

Using the atomic force microscope (AFM) *in situ* during the crystallization of the protein apoferritin, we show that for this system the kink density along the steps is an equilibrium property that, multiplied by the frequency of molecular attachment, fully determines the propagation of growth steps. The intermolecular bond energy is  $3.2k_B T$ . Point defects are nonequilibrium and are caused by incorporation of impurity molecules, and replicate in subsequent layers due to the strain they cause. Using single-molecule manipulation with the AFM tip, the defects can be healed to restore the regular lattice.

PACS numbers: 81.10.Aj, 61.16.Ch, 61.72.Ji, 87.15.Nn

Crystallization, which underlies water freezing in clouds and oceans, magma solidification in the Earth's interior, growth of semiconductor boules and epitaxial layers, and various other natural and technological processes, occur by ordered addition of atoms or molecules. Recently, phenomena related to the formation of surface structures and growth of epitaxial layers under ultrahigh vacuum [1,2] or during crystallization of proteins have been monitored with resolution approaching the size of the species that build the crystal.

For studies of the molecular mechanisms of crystal growth from supersaturated environments, we chose crystallization of apoferritin [3]. Apoferritin molecules are quasispherical and crystallize in a face-centered cubic (fcc) lattice [3]. Octahedral {111} faces dominate the crystal habit. Growth from solution purified by gel filtration [4] occurs by spreading of layers generated by surface nucleation similar to other proteins [5–7]. In our experiments, the crystals grew [4] on a glass substrate at  $23.0 \pm 0.3$  °C in the atomic-force microscopy (AFM) fluid cell. Tapping-mode AFM images of the crystal surface were collected *in situ* during the growth. The scanning parameters were adjusted such that continuous imaging affected neither the surface structure, nor the process dynamics. For further evidence, see the discussion of Fig. 2 below. Supersaturation  $\sigma$ , defined as chemical potential difference  $\Delta\mu$  (in  $k_B T$  units) between solution and crystal, was determined from the actual and equilibrium solution concentrations,  $C$  and  $C_e$ :  $\sigma \equiv \Delta\mu/k_B T = \ln(C/C_e)$ . This  $C_e = 23 \pm 3 \mu\text{g}/\text{cm}^3 = 3.2 \times 10^{13}$  molecules/ $\text{cm}^3$  was determined as  $C$  at which long steps stopped moving before retreating at  $C < C_e$ .

The structures of a (111) crystal face and of a growth step are shown in Fig. 1. In Fig. 1(a) and in all other images the periodicity within a molecular row is 13 nm and the layer thickness is 10.5 nm, in agreement with the x-ray structure [3].

Solute molecules attach to the crystal predominantly at kinks along a step [8]. Hence, the kink density is a fundamental variable that characterizes the ability of the crys-

tal to incorporate solute molecules [9,10]. From images similar to Fig. 1(a), we determine the kink density along a step by counting the molecules between two kinks,  $n_k$  [11]. The distributions of  $n_k$  for three supersaturations that include near equilibrium and a very high value are shown in Fig. 1(b). They are nearly identical, and we conclude

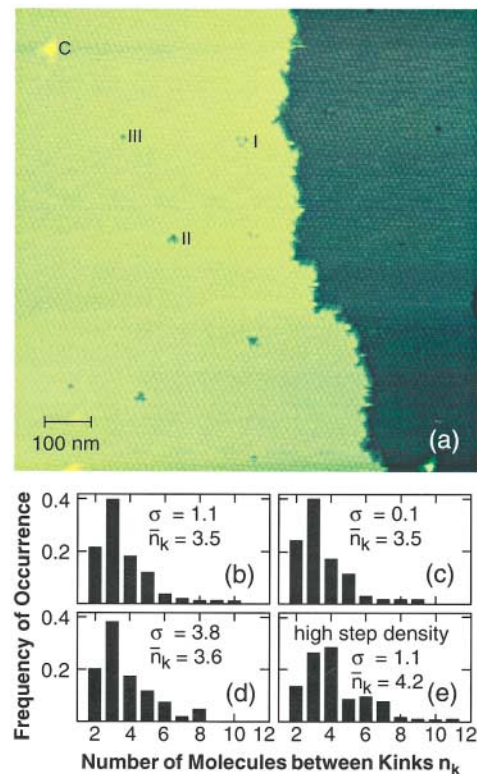


FIG. 1 (color). Steps and kinks. (a) Growth step at supersaturation  $\sigma = 1.1$ . Dark green: lower layer; yellow: advancing upper layer. Examples of adsorbed clusters and defects of types I, II, and III are marked. (b)–(d) Distribution of molecules between kinks on steps located  $>0.5 \mu\text{m}$  apart, obtained from images similar to (a) at the three supersaturations indicated in the plots, the mean values of the distributions for each case are also shown. (e) Same as (b), with steps as close as 7–10 molecules ( $0.1\text{--}0.3 \mu\text{m}$ ) apart.

that kinks are not created by nucleation of molecular rows along a step. Hence, the equilibrium value of kink density  $1/n_k$  is determined by the balance of molecular interactions and thermal fluctuations in the top crystal layer [1,12,13]. The average  $\bar{n}_k$  depends on the energy needed to create a kink  $w$  as [9]

$$\bar{n}_k = \frac{1}{2} \exp(w/k_B T) + 1. \quad (1)$$

From the value of  $\bar{n}_k$  in Figs. 1(b)–1(d),  $w = 1.6k_B T$ , somewhat lower than  $w$  for Si(001) [14]. If we assume first-neighbor interactions only, we can evaluate the intermolecular bond energy,  $\phi$ . When a molecule is moved from within the step on a (111) face of a fcc crystal to a location at the step, 4 kinks are created, 7 bonds are broken, and 5 are formed [8]. Then,  $w = \phi/2$  and  $\phi = 3.2k_B T$ . Some of the protein-protein interactions, e.g., electrostatic, may have a range longer than the molecular dimension [15]. Accounting for second and third neighbor contributions to  $w$ ,  $\phi$  must be lowered by at most 10% [16].

Figure 1(e) shows the distribution of  $n_k$  along steps spaced about 10 molecules ( $0.13 \mu\text{m}$ ) apart, as opposed to  $0.5$  to  $1 \mu\text{m}$  in Figs. 1(b)–1(d). The kink density and step meandering are lower. This indicates step-step repulsion [17], which may come from the entropy loss of closely spaced steps [11,18], or overlapping of the relaxation elastic fields of neighboring step edges [19,20].

During step motion, segments deviating from the dense [110] crystallographic directions rush forward because of their higher kink density [9] and taper off. Thus, step motion is determined by the kink density along the dense directions.

The kinetics of incorporation are reflected by the flux of molecules into a growth site. To monitor these fast incorporation events, we disabled the slow scanning axis of the AFM [1]. The advance of a step site is shown in Fig. 2(a). Figure 2(b) shows that the chosen scanning parameters ensured that step propagation was not affected by scanning over the same line for  $\sim 3$  min. Although the solution is supersaturated, the time trace in Fig. 2(a) reveals not only 25 arrivals to but also 22 departures of molecules from the monitored site, evidencing the selectivity of the crystal growth process. The residence times  $\tau$  between these events fall into  $\tau \leq 1$  s or  $t > 5$  s. In Fig. 2(a) we have 6 events of the second type and 19 events of the first. Their ratio is roughly equal to the kink density along the step, suggesting that the long-time events may be attachments/detachments to/from a kink, while the short ones may be sightings of molecules at the step edge.

Since we do not see the neighboring sites on the step, we cannot distinguish between events due to molecular diffusion along the step or to exchange with either the terrace between the steps or the adjacent solution. For this, we calculated the time correlation function of the step position  $x$  (in molecular size units) as  $\langle [x(t + \Delta t) - x(t)]^2 \rangle_{\Delta t}$ , with averaging over the respective  $\Delta t$ , and plotted it in Fig. 2(c) as a function of  $\Delta t$ . Theoretical analyses of the exchange of the steps with the medium at equilibrium

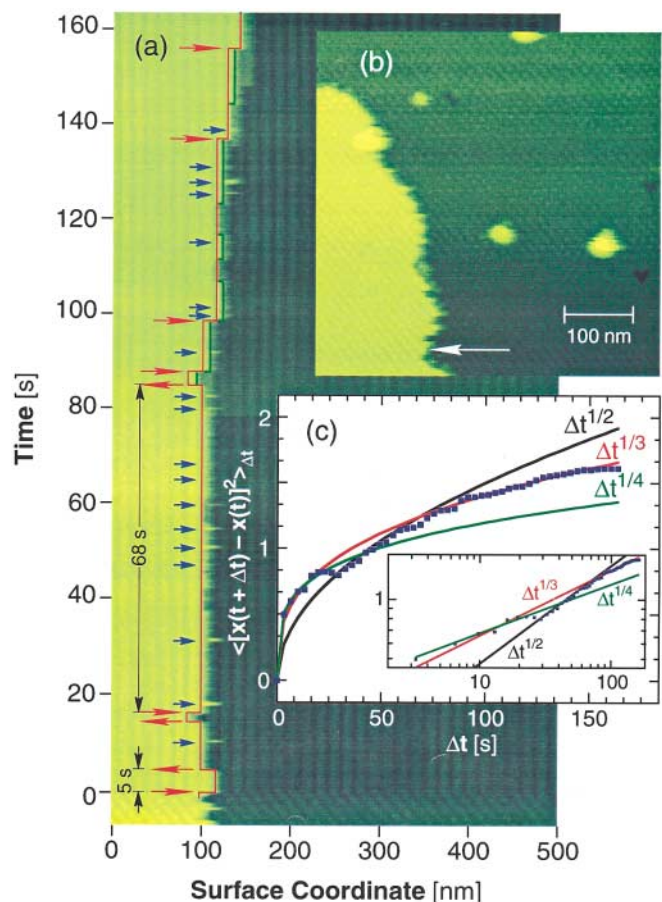


FIG. 2 (color). Incorporation of molecules into steps at  $\sigma = 1.1$ . (a) Pseudocolor image recorded with the  $Y$  scan axis disabled at time = 0 [1,12] shows displacement of one step site. Red contour traces step position. Arrows indicate attachment and detachment events; for details, see text. Appearance of  $\frac{1}{2}$  molecule attachments at times  $> 80$  s, highlighted in green, is due to events at a neighboring site that enter image due to scanner drift. (b) Surface scan immediately after (a); arrow indicates location of monitoring in (a). (c) Time correlation curve corresponding to the trace in (a); inset: logarithmic plot.

[13,21] predict that if diffusion along the step edge dominates the advance of the step site, the cross correlation should follow  $\Delta t^{1/4}$  dependence [13,21]. We found no theory dealing with supersaturated conditions. However, motion of a site on the step edge is similar to Brownian motion [21]. For Brownian diffusion, the coefficient relating  $\langle [x(t + \Delta t) - x(t)]^2 \rangle_{\Delta t}$  and  $\Delta t^{1/2}$  may vary, but the exponent  $\frac{1}{2}$  of  $\Delta t$  does not depend on the presence or absence of concentration/chemical potential gradients [22]. Hence, we use only the exponents of  $\Delta t$  stemming from the data in Fig. 2(c) for further discussion.

The data in Figs. 2(c) do not fit a single exponential. The deviation from  $\frac{1}{4}$  at times longer than 20 s allows us to conclude that the trace in Fig. 2(a) likely reflects exchange of molecules between the step and interstep terraces or the adjacent solution [12,17,21]. Hence, from the net attachment of 3 molecules for 162 s and the probability of viewing a kink of  $1/\bar{n}_k = 1/3.5$ , we get  $f = 0.065 \text{ s}^{-1}$ ,

or one molecule per 15 s. Thus, even at the relatively high  $\sigma = 1.1$ , incorporation of molecules into the crystal is extremely slow and occurs over macroscopic time scales.

Incorporation of molecules into growth sites results in step propagation. The step velocities averaged over image collection times of  $\sim 40$ – $50$  s are shown in Fig. 3. The first four data sets fit well the proportionality

$$v = \beta \Omega C_e (C/C_e - 1), \quad (2)$$

where  $\Omega$  is the crystal volume per molecule. For the fcc apoferritin crystals with a lattice constant  $a = 18.4$  nm [3],  $\Omega = \frac{1}{4}a^3 = 1.56 \times 10^{-18}$  cm<sup>3</sup>. The averaged step kinetic coefficient, or the macroscopic kinetic constant of growth from Eq. (2), is  $\beta = 6 \times 10^{-4}$  cm/s. This is comparable to values of other, faster growing proteins, indicating that the low net molecular attachment flux and step velocities of this protein are due to the low solution concentration, reflected in the molecular density ratio between the solution and crystal,  $\Omega C_e = 5 \times 10^{-5}$ . From Fig. 3, the average step velocity at  $(C/C_e - 1) = 2$ ,  $\sigma = 1.1$ , is  $v = 0.26$  nm/s. The product  $a(1/\bar{n}_k)f$  determined at the same conditions should equal this step velocity. Substituting, we get 0.24 nm/s. The closeness of the predicted and actual values indicates that: (i) incorporation into the monitored site in Fig. 2(a) was not affected by the continuous scanning; (ii) kink density along the dense crystallographic directions and net frequency of attachment to a kink are the fundamental variables that fully determine the step propagation during crystal growth.

Figure 1(a) shows the presence of clusters and three kinds of surface point defects: trivacancy with a cluster, trivacancy, and vacancy. These point defects are typical for the  $\{111\}$  apoferritin faces, and we label them, respectively, types I, II, and III. In Fig. 4, we monitor the

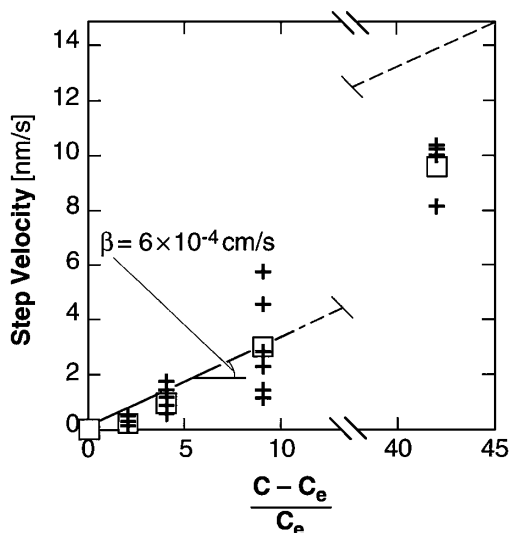


FIG. 3. Step velocities determined by comparing step positions within 44–47 s, plotted as a function of concentration supersaturation  $(C - C_e)C_e^{-1}$ . The data scatter reflects the stochastic nature of crystal growth at the molecular level. Solid line corresponds to shown step kinetic coefficient.

interactions between two advancing steps and these surface features. Figure 4(a) shows two clusters adsorbed on the lower terrace, identified in another study as apoferritin dimers shaped as two bound monomer spheres [23], and present in the growth solution at about 5% of the dry protein mass [4]. The dimers occupy three, rather than two, monomer lattice sites likely due to noncrystallographic contacts between the monomers within a dimer.

The lower terrace also contains a type I and a type III defect. The type I defect locally retards the approaching step and eventually a channel with the defect at the far end is formed; Fig. 4(b). This channel does not close until a certain critical number of molecules in the steps forming the channel,  $n^*$ , is reached. For this and other series of images at  $\sigma = 1.6$ , the value of  $n^*$  that occurred most frequently was 4. At  $\sigma = 1.1$  the most frequently occurring  $n^*$  increased to 6, i.e.,  $n^*$  roughly scales with  $1/\sigma$ . This appears to suggest that the short steps are retained because of the excess energy associated with the unsaturated bonds of the terminal molecule. However, substituting the  $n^*$ 's in the discrete Gibbs-Thomson relation  $\Delta\mu = \phi/n^*$  [24,25] and using the above  $\phi$ , we get  $\Delta\mu$  values about half of the actual ones. This suggests that the elastic strain introduced by the impurity cluster may also affect the behavior of the steps around the cluster.

Steps longer than  $n^*$  are not hindered by the capillary and elastic barriers and move to close the channel in Fig. 4(c). However, the elastic field does not allow molecules to attach on top of the type I defect, and a type II defect is created in the next layer, Figs. 4(c)–4(e). Cluster C2 is pushed away by the step. The type III defect next to it in Fig. 4(a), after some configurational variations in Figs. 4(b)–4(d), is replicated in the advancing layer, Fig. 4(f). Figure 4(f) also shows that the third layer is

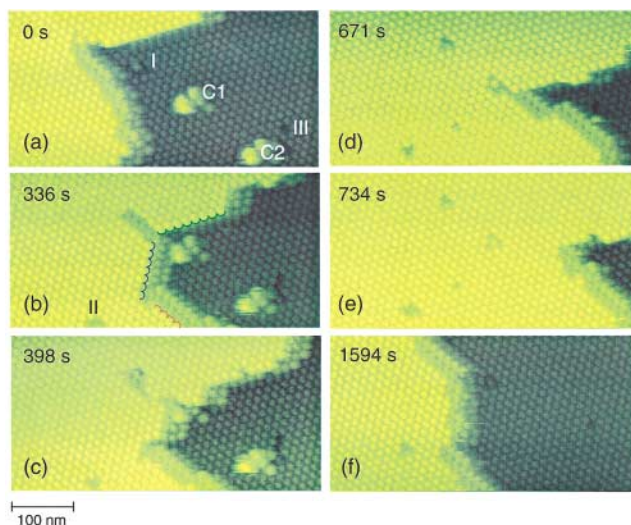


FIG. 4 (color). Creation and evolution of defects at supersaturation  $\sigma = 1.6$ . (a)–(e) Interactions between advancing step and types I and III defects and two clusters, C1 and C2. (f) A new step is stopped by types I, II, and III vacancies; a type II vacancy is created in the new layer on top of the first seen in (b) after a shift of the view field.

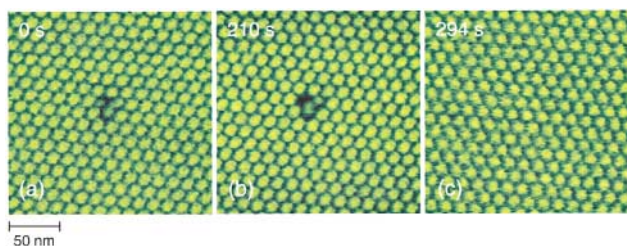


FIG. 5 (color). Defect manipulation by the AFM tip. (a) Type I defect with an incorporated molecular fragment sometimes present in apoferritin solutions [4]. (b),(c) After two hits by the AFM tip perfect crystal lattice is restored.

retarded by all the defects in the second layer and the type II defect in the second layer in Fig. 4(b) is also replicated in the third layer.

Thus, Fig. 4 illustrates the series of transformations: cluster  $\rightarrow$  type I  $\rightarrow$  type II in subsequent crystal layers. In numerous similar image sequences, we found that type I and type II may produce a type III defect and types II and III often replicate in the next layer. A column of type III vacancies may be terminated by the incorporation of a molecule. The resulting average length of these bottle-shaped cavities is about five crystal layers. Note that we never saw point defects that were not initiated by a cluster adsorbed on the crystal surface. Unlike Schottky and Frenkel defects [26], none of the defects observed here are equilibrium defects induced by the thermal vibrations of the lattice molecules and their lattice sites have never been occupied by apoferritin monomer molecules. Since they are bound to the incorporated cluster, these defects possess no translational mobility.

If adsorption of molecular clusters on the growth interface is reduced, the concentration of types I, II, and III defects in the crystal will be significantly lower. However, in view of the limited capabilities of the biochemical purification techniques to achieve purity levels anywhere close to those in semiconductor growth [27], it is obvious that such defects will always be created. Hence, a means to control defect content during crystals' growth is needed. As a proof of concept of possibility to manipulate individual defects, we applied a nanolithographic procedure. Figure 5(a) shows a trivacancy containing a cluster and a molecular fragment. Between Figs. 5(a) and 5(b), the AFM tip was activated to push the defect for several milliseconds. Figure 5(b) shows that the smaller molecular fragment is removed. A second hit between Figs. 4(b) and 4(c) removes the cluster causing this defect, and the lattice is healed, Fig. 5(c).

We thank J. W. M. Frenken, A. A. Chernov, M. Giesen, A. Ostrogorsky, D. Petsev, N. A. Booth, and R. M. Banish for references, discussions, and suggestions, and L. Carver for expert work on the figures. This work was supported by NHLBI, NIH (Grant No. RO1-HL 58038) and OLMSA, NASA (Grants No. NAG8-1354 and No. 97 HEDS-02-50).

\*Corresponding author.

Email address: peter@cmmr.uah.edu

- [1] See, for instance N. Kitamura, M. G. Lagally, and M. B. Webb, *Phys. Rev. Lett.* **71**, 2081 (1993).
- [2] B. S. Swartzentruber, *J. Cryst. Growth* **188**, 1 (1998); B. Voightlaender and M. Kaestner, *Phys. Rev. Lett.* **81**, 858 (1998); Y. G. Kuznetsov *et al.*, *Surf. Sci.* **440**, 69 (1999).
- [3] D. M. Lawson *et al.*, *Nature (London)* **349**, 541 (1991); P. D. Hempstead *et al.*, *J. Mol. Biol.* **268**, 424 (1997).
- [4] B. R. Thomas, D. Carter, and F. Rosenberger, *J. Cryst. Growth* **187**, 499 (1997).
- [5] A. J. Malkin *et al.*, *Nat. Struct. Biol.* **2**, 956 (1996).
- [6] P. G. Vekilov and J. I. D. Alexander, *Chem. Rev.* (to be published), and refs. therein.
- [7] A. J. Malkin *et al.*, *J. Phys. Chem.* **100**, 11 736 (1996), and other papers by these authors.
- [8] I. N. Stranski, *Z. Phys. Chem.* **136**, 259 (1928); R. Kaischew, *Z. Phys.* **102**, 684 (1936).
- [9] W. K. Burton, N. Cabrera, and F. C. Frank, *Philos. Trans. R. Soc. London A* **243**, 299 (1951).
- [10] A. A. Chernov, *Modern Crystallography III: Growth of Crystals* (Springer, Berlin, 1984).
- [11] E. D. Williams and N. C. Bartelt, *Science* **251**, 393 (1991).
- [12] J. W. Gibbs, *The Collected Works of J. W. Gibbs* (Yale University Press, New Haven, 1961).
- [13] M. Poensgen *et al.*, *Surf. Sci.* **274**, 430 (1992); L. Kuipers, M. Hoogeman, and J. Frenken, *Phys. Rev. Lett.* **71**, 3517 (1993); L. Kuipers, M. S. Hoogeman, and J. W. M. Frenken, *Phys. Rev. B* **52**, 11 387 (1995).
- [14] B. S. Swartzentruber *et al.*, *Phys. Rev. Lett.* **65**, 1913 (1990).
- [15] B. Beresford-Smith, D. Y. C. Chan, and D. J. Mitchell, *J. Colloid Interface Sci.* **105**, 216 (1985).
- [16] D. N. Petsev and P. G. Vekilov (unpublished).
- [17] C. Alfonso, J. M. Bermond, J. C. Heyraud, and J. J. Metois, *Surf. Sci.* **262**, 371 (1992); N. C. Bartelt, T. L. Einstein, and E. D. Williams, *Surf. Sci. Lett.* **240**, L591 (1990).
- [18] D. J. Wolf and J. A. Jaszczak, *Surf. Sci.* **277**, 301 (1992).
- [19] V. I. Marchenko and A. Y. Parshin, *Sov. Phys. JETP* **52**, 129 (1980).
- [20] B. Houssmandzadeh and C. Misbah, *J. Phys. I (France)* **5**, 685 (1995).
- [21] A. Pimpinelli *et al.*, *Surf. Sci.* **295**, 143 (1993); T. Ihle, C. Misbah, and O. Pierre-Louis, *Phys. Rev. B* **58**, 2289 (1998), and refs. therein.
- [22] P. N. Pusey and R. J. Tough, in *Dynamic Light Scattering*, edited by R. Pecora (Plenum Press, New York, 1985); P. Atkins, *Physical Chemistry* (Freeman, New York, 1998), p. 754.
- [23] P. M. Harrison and P. Arosio, *Biochim. Biophys. Acta* **1275**, 161 (1996).
- [24] I. N. Stranski and R. Kaischew, *Z. Phys. Chem. B* **26**, 100 (1934).
- [25] R. Kaischew and I. N. Stranski, *Z. Phys. Chem. B* **35**, 427 (1937).
- [26] C. Kittel, *Introduction to Solid State Physics* (John Wiley and Sons, New York, 1986).
- [27] H. J. Queisser and E. E. Haller, *Science* **281**, 945 (1998).